Available online at www.sciencedirect.com

ScienceDirect

Advances in Space Research 76 (2025) 718–733

ADVANCES IN SPACE RESEARCH (a COSPAR publication)

www.elsevier.com/locate/asr

Crustal stability and hazard assessment along the Xinjiang-Tibet Railway by GNSS and gravity data

Jie Liu [a], Sen Kong [a], Shuanggen Jin [a,b,*], Yunlong Zhang [c], Xinqi Liu [a], Shengkun Nie [a], Keke Xu [a]

[a] School of Surveying and Land Information Engineering, Henan Polytechnic University, Jiaozuo 454003, China
[b] Shanghai Astronomical Observatory, Chinese Academy of Sciences, Shanghai 200030, China
[c] Academy of Geomatics and Geographic Information, China Railway Design Corporation, Tianjin 300308, China

Received 3 January 2025; received in revised form 9 April 2025; accepted 7 May 2025
Available online 13 May 2025

Abstract

The Tibetan Plateau represents one of the most seismically active regions globally. The construction of the Xinjiang-Tibet Railway is profoundly affected by crustal deformation and geological hazards. To address the urgent need for regional crustal stability and risk assessment in this region, this study integrates large-scale observations from the Gravity Recovery and Climate Experiment (GRACE) satellite and GNSS data to extract vertical crustal deformation information along the railway route, along with multi-source geological, seismic, and meteorological data. Additionally, terrestrial water storage changes are a critical factor influencing stability. A multi-factor weighted overlay method is employed, incorporating ten evaluation indicators to assess crustal stability along the railway and develop a multidimensional framework for monitoring and evaluating regional crustal stability. The study also extends the research area by 40 km, 80 km, and 170 km. The assessment results reveal that Equivalent Water Height (EWH) variations, derived from GRACE satellite gravimetry, demonstrate relatively stable interannual fluctuations across the study region, while Terrestrial Water Storage Anomalies (TWSA) exhibit a modest declining trend, which amplifies with increasing spatial scale. Integrating GRACE satellite gravimetry and GNSS-derived deformation metrics, this study evaluates crustal stability indices and categorizes the study area into stable, moderately stable, and moderately unstable zones, highlighting spatial variations in regional tectonic stability. The northern section of the Xinjiang-Tibet Railway predominantly features stable to moderately stable conditions. In contrast, the southern section shows moderately unstable to unstable conditions, with instability expanding as the scope of analysis broadens. This evaluation framework offers critical insights and scientific support for infrastructure development and disaster mitigation strategies.

Keywords: Xinjiang-Tibet Railway; GRACE; Crustal stability; Multi-factor weighted overlay method

1. Introduction

The Xinjiang-Tibet Railway is located at the southwestern border of China and the southwestern margin of the Tibetan Plateau, spanning three prefectures across 13 counties (districts) in Xinjiang and Tibet, with a total length of approximately 2,000 km. The stability and safety

* Corresponding author at: School of Surveying and Land Information Engineering, Henan Polytechnic University, Jiaozuo 454003, China.
E-mail addresses: liujie2016@hpu.edu.cn (J. Liu), kongsen0622@163.com (S. Kong), sgjin@shao.ac.cn (S. Jin), zhangyunlong@crdc.com (Y. Zhang), liuxinqi0310@163.com (X. Liu), 212004020058@home.hpu.edu.cn (S. Nie), xkk@hpu.edu.cn (K. Xu).

https://doi.org/10.1016/j.asr.2025.05.021

of the railway are predominantly shaped by geomorphological conditions, including high mountains and deep valleys, and by endogenic geological factors such as high stress, active faulting, seismic activity, and complex lithological assemblages (Zhang et al., 2013; Zhang et al., 2022). The extreme regional geological background—featuring high altitude, periglacial conditions, high stress, intense seismicity, elevated geothermal gradients, and active neotectonic movements—necessitates urgent monitoring of regional crustal deformation and hazard evaluation along the railway route.

The monitoring and evaluation of crustal stability constitute an emerging field in Earth sciences. Traditionally, regional crustal stability assessments have incorporated geological, geophysical, geochemical, hydrogeological, geomorphological, and seismic factors, along with crustal deformation and environmental geology (Dang et al., 2017; Xu et al., 2020). In recent years, advanced satellite geodetic techniques, including Global Navigation Satellite System (GNSS) and satellite gravimetry, have generated a new generation of geodetic products with enhanced observational accuracy, spatiotemporal resolution, and significant improvements in long-term monitoring capabilities (Eshagh et al., 2024; Heki and Jin, 2023; Pan et al., 2023; Jin et al., 2005, 2010, 2022, 2024). These techniques deliver high-precision surface and gravity field change data, establishing themselves as indispensable tools for understanding the dynamics of active continental blocks and monitoring subsidence in critical regions (Rao and Sun, 2020; Chen et al., 2022; Zhao et al., 2017).

Modern geodesy, in this context, surpasses traditional geomechanical theories by integrating multi-source observational data to enhance the monitoring and evaluation of geological stability. For instance, Franklin and Huang (2022) applied GNSS and interferometric synthetic aperture radar (InSAR) data to analyze interseismic crustal deformation and horizontal strain rates in Taiwan. Their findings revealed significant deformation along the plate boundary between the Philippine Sea Plate and the Eurasian Plate. However, the study faced limitations in spatial resolution and excluded anthropogenic subsidence from its analysis. Similarly, Liu et al. (2023) proposed a multidimensional crustal stability monitoring framework for the Red River Fault Zone by combining dense GNSS observational data with surface deformation and fault activity. However, it lacks the tracking of long-term, large-scale data on crustal stability changes, which makes it unable to fully assess the impact of groundwater storage on crustal stability, especially in regions with significant hydrological changes. Yao et al. (2021) assessed the crustal stability of the eastern Tibetan Plateau using geomechanics and continental dynamics, providing foundational support for major engineering projects. However, the study is limited by scarce observational data and lacks a detailed discussion on the distribution, types, and interactions of specific disasters. It also fails to consider other factors that may affect crustal stability. Xu et al. (2023) integrated GNSS, levelling, and InSAR observations to construct a three-dimensional deformation field of the Tibetan Plateau, facilitating detailed assessments of seismic hazards along active faults within the region. Wu (2024) studied crustal stability from tectonic and surface stability perspectives, developing an evaluation method for the Bailongjiang River Basin by combining factor analysis and fuzzy mathematics with a membership function approach. However, the evaluation is static and lacks a dynamic adjustment mechanism for the indicators. Additionally, due to the region's complex geological conditions, some data were missing.

This study integrates long-term geological, seismic, and geodetic datasets by combining GNSS observations and gravity-derived measurements to incorporate terrestrial water storage (TWS) variations into surface monitoring data. The researchers developed a multidimensional monitoring and evaluation framework that employs factor analysis to objectively assign weights and quantitatively assess crustal stability along the Xinjiang-Tibet Railway. Considering the unique environmental conditions of the Tibetan Plateau, the study applies satellite gravimetry to detect large-scale spatial TWS variations. Unlike earlier studies that focused mainly on traditional evaluation factors, this research introduces TWS variations into crustal stability assessments for the first time. Weight analysis reveals that TWS variations critically influence crustal stability. Moreover, satellite gravimetry identifies minimal TWS changes along the railway route, supporting the conclusion that the region's crust is stable. This framework overcomes key limitations in earlier stability evaluations of the Tibetan Plateau, such as insufficient data, narrow evaluation criteria, and subjective weight allocation. The results deliver accurate, high-resolution, and timely surface deformation data, enabling precise and reliable stability assessments. These findings provide valuable insights for urban development, infrastructure planning, major project siting, and safety evaluations in Xinjiang and Tibet.

2. Data and methods

2.1. Study data

This study evaluates the crustal stability of the Xinjiang-Tibet Railway region in defining study areas extending 40 km, 80 km, and 170 km outward from the railway (Fig. 1). Ten evaluation indicators are selected: maximum shear strain rate, the dilatation rate, earthquake magnitude, peak ground acceleration (PGA), Bouguer gravity anomalies, active faults, river system development, slope gradient, average annual precipitation, and equivalent water height (EWH).

We employ 240 GNSS regional stations from the China Crustal Movement Observation Network (CMONC) from 1999 to 2017, along with continuous reference station data from the southeastern edge of the Tibetan Plateau. We applied GAMIT/GLOBK 10.4 and QOCA software to estimate station positions and velocities. We generated a

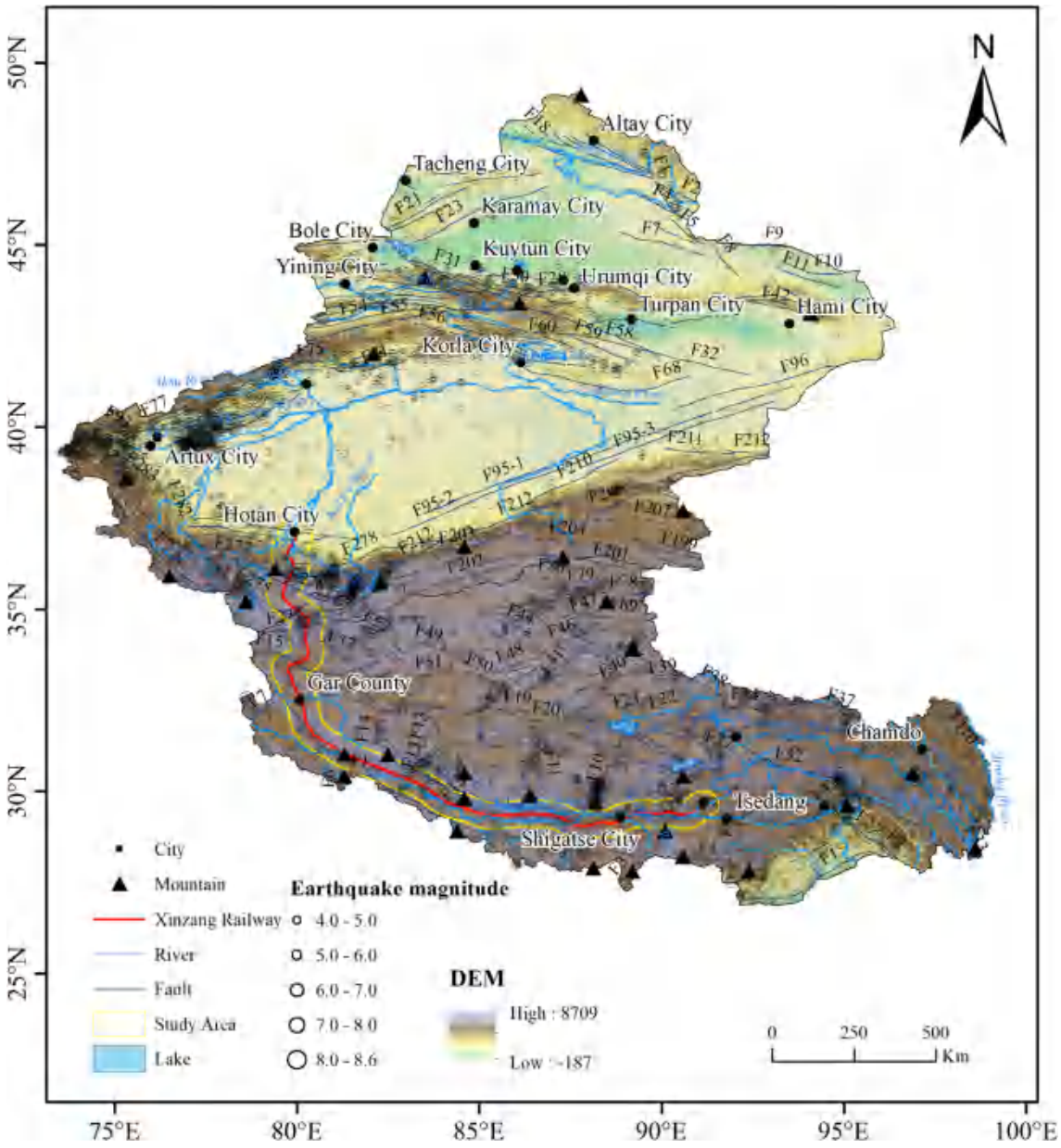

Fig. 1. Topographic Map of the Study Area.

unified velocity field using ITRF2014 as the reference frame and then transformed it into a relatively stable reference frame for the Eurasian region. Stations exhibiting significant motion trends or large discrepancies in velocity were excluded from the analysis, and the final velocity results had an average error of less than 1 mm/a. The maximum shear strain rate and the dilatation rate of the southeastern Tibetan Plateau were calculated using the spherical wavelet method, with the results cropped to match the study area. These results align with the conclusions of Xu et al. (2020). Earthquake magnitude data, spanning from 183 BCE to 2023 CE, were retrieved from the National Earth System Science Data Center (https://www.geodata.cn). Peak ground acceleration values were extracted and vectorized from the China Seismic Ground Motion Parameter Zoning Map (1:4,000,000) using the ArcGIS platform. Bouguer gravity anomalies were obtained from the nationwide Bouguer Gravity Anomaly Map (1:4,000,000), compiled by the China Earthquake Administration in 2011. Active fault data were sourced from the Fifth Generation Seismic Zoning Map (1:2,500,000). River system development was analyzed through Euclidean distance buffering, based on 1:50,000 topographic maps.

Precipitation data were synthesized from monthly precipitation datasets at 1-km resolution spanning from 1901–2022. We employ GRACE Mascon products to represent TWS anomalies relative to the 2004–2009 mean baseline, typically expressed as EWH. Cubic spline

interpolation was used to fill in missing months. The CSR and JPL Mascon data were then averaged to improve the accuracy of terrestrial water storage change information.

2.2. Crustal stability ananalysis methods

To accurately evaluate regional crustal stability, it's important to consider various factors to obtain reliable and comprehensive results. This study uses a statistical analysis to determine the weights of each factor and reduce correlations between them. Then, the crustal stability of the area is assessed using a multi-factor weighted overlay approach.

The evaluation process begins by classifying influencing factors, grouping highly correlated and closely related factors into the same category while maintaining a low correlation between different categories. Each category functions as a common factor, enabling the quantitative evaluation of regional geological stability by expressing the total influence as the sum of linear functions of common and specific factors(Dang et al., 2017). Let all observed variables be defined as: $X = [(X_1, X_2, ..., X_P)]^T$, where P represents the total number of variables, and the following relationship holds:

$$X_i = l_i + a_{i1}f_1 + a_{i2}f_2 + ... + a_{im}f_m + e_i \quad (1)$$

where: l_i represents the mean of X_i; f_i represents the common factors, where m is the total number of factors; e_i is the specific factor; a_{ij} denotes the correlation coefficient between X_i and f_i.

Then we standardize X_i such that it has a mean of 0 and variance of 1. The standardized model is as follows:

$$X_i = a_{i1}f_1 + a_{i2}f_2 + ... + a_{im}f_m + e_i \quad (2)$$

The next step is to generate the correlation matrix. We define A as the factor loading matrix, $A = [a_{ij}]$, where $i = 1, 2, \ldots, m$, and the correlation matrix R is expressed as:

$$R = \begin{bmatrix} r_{11}r_{12}\cdots r_{1p} \\ r_{21}r_{22}\cdots r_{2p} \\ \vdots\vdots \\ r_{p1}r_{p2}\cdots r_{pp} \end{bmatrix} \quad (3)$$

We calculate the eigenvalue $k_1, k_2, ..., k_P$ and their corresponding standardized orthogonal eigenvectors of the correlation matrix R, and compute the factor loadings a_{ij} using the formula:

$$a_{ij} = \sqrt{k_i}a_{ij} \quad (4)$$

The factor score coefficients b_{ij} are calculated using the regression method, substituting the load matrix A into the regression formula.

Compute the factor scores using the following formula:

$$score(n, j) = b_{j1}X_{1n} + b_{j2}X_{2n} + \cdots + b_{jp}X_{pn} \quad (5)$$

The crustal stability index K is derived using the multi-factor weighted overlay method and is expressed as:

$$K = \sum_{i=1}^{p} L_i w_i \quad (6)$$

where K is the regional crust stability index; L_i represents the evaluation indicators; w_i denotes the weights of the evaluation indicators.

2.3. Strain field estimation

The GNSS velocity field reflects crustal movement on a macro scale but lacks detailed information about deformation intensity. While the velocity field varies under different reference frames, the strain field is reference-frame independent and has a direct mechanical relationship with tectonic stress. This characteristic enables the strain field to visually represent the spatial distribution of stress and strain in a region, which is closely associated with seismic activity. In this study, the strain field is calculated using the spherical wavelet method. Spherical wavelets generalize traditional wavelets from an infinite plane to a finite sphere. They represent a cutting-edge research tool in wavelet analysis and are widely applied in fields such as geomagnetism and gravity studies. The Gaussian difference spherical wavelet (Difference of Gaussians, DOG) function at any point P on a unit sphere with a radius of 1 can be expressed as follows (Bogdanova et al., 2005):

$$\begin{aligned} g = &\sqrt{\frac{4a^2}{((a^2-1)\cos c+(a^2+1))^2}}\exp\left(-\frac{\tan^2(c/2)}{a^2}\right) \\ &-\frac{1}{a}\sqrt{\frac{4a^2}{((a^2-1)\cos c+(a^2+1))^2}}\exp\left(-\frac{\tan^2(c/2)}{aa}\right) \end{aligned} \quad (7)$$

in this equation, c is the angular distance between the observation vector and the wavelet center $0 \leq c \leq 180^\circ$; $a = 2^{-q}$, q represents the scale, and as the scale increases, the value decreases. The value a is 1.25. Based on the motion velocities of the crust in the N, E, and U directions, a function model of the spherical wavelet can be constructed (Xu et al., 2020):

$$\begin{aligned} \mathbb{m}_N^i(k_i, u_i) &= \sum_{k=q_{min}}^{k=q_{max}} a_k g_k(k_i, u_i) + e_N^i, P_N^i \\ \mathbb{m}_E^i(k_i, u_i) &= \sum_{k=q_{min}}^{k=q_{max}} b_k g_k(k_i, u_i) + e_E^i, P_E^i \\ \mathbb{m}_U^i(k_i, u_i) &= \sum_{k=q_{min}}^{k=q_{max}} c_k g_k(k_i, u_i) + e_U^i, P_U^i \end{aligned} \quad (8)$$

In the above equation, k_i, u_i is the longitude and latitude of observation station $i, i = 1, \cdots, n$; $g_k(k_i, u_i)$ is the k-th wavelet basis function of GNSS station (k_i, u_i);a_k, b_k, c_k are the wavelet coefficients to be determined; e_N^i, e_E^i, e_U^i are the observation noises in the three directions; P_N^i, P_E^i, P_U^i are the observation weight matrices in the three directions, determined by the accuracy of the velocity estimated from the GNSS station.

2.4. Equivalent water height estimation

The Tibetan Plateau is renowned for its vast permafrost, and variations in water volume are indicative of permafrost thawing, which subsequently provides insights into regional stability. To examine the variations in water storage along the Xinjiang-Tibet Railway, we employ the GRACE and GRACE-FO RL06 Mascon products, provided by the CSR at the University of Texas and NASA's JPL, covering the period from January 2004 to December 2021.

Compared to traditional spherical harmonic data, the Mascon products offer several advantages, the most significant of which is the absence of the need for additional post-processing, which has led to their widespread application. Since the spatial resolution of the CSR Mascon and JPL Mascon products is 0.25° × 0.25° and 0.5° × 0.5°, respectively, the JPL Mascon product was resampled to 0.25° × 0.25° to ensure consistent spatial resolution between the two datasets.

3. Results and analysis

3.1. Crustal stability monitoring and hazard assessment

When studying crustal stability along the Xinjiang-Tibet Railway, the primary factors influencing regional crustal stability are endogenic factors, exogenic factors, and medium conditions. Among the exogenic factors, geological hazards are the most direct and significant (Yao et al., 2021). This study evaluates stability using 5 primary indicators, as shown in Table 1, with TWS identified as a key influencing factor. Then, each primary factor is further divided into several secondary factors.

Before performing factor analysis, calculating the Kaiser-Meyer-Olkin (KMO) value is essential to assess the data's suitability. The KMO statistic measures the strength of correlations and partial correlations between variables, with values ranging from 0 to 1. A KMO close to 1 indicates strong suitability for factor analysis, while a KMO close to 0 suggests unsuitability. Values between 0.5 and 0.7 warrant cautious acceptance. In this study, the KMO values for the 40 km, 80 km, and 170 km ranges are 0.656, 0.637, and 0.668, respectively, indicating that the data are suitable for factor analysis.

We calculate the weights for different regional extents (Table 1) using the 40 km region along the Xinjiang-Tibet Railway as an example. For the 80 km region along the railway, the weight distribution is as follows: active faults account for 0.0523, Bouguer gravity anomaly for 0.0611, historical earthquake magnitude for 0.0776, peak ground acceleration for 0.0257, maximum shear strain rate for 0.1302, the dilatation rate for 0.1242, slope gradient for

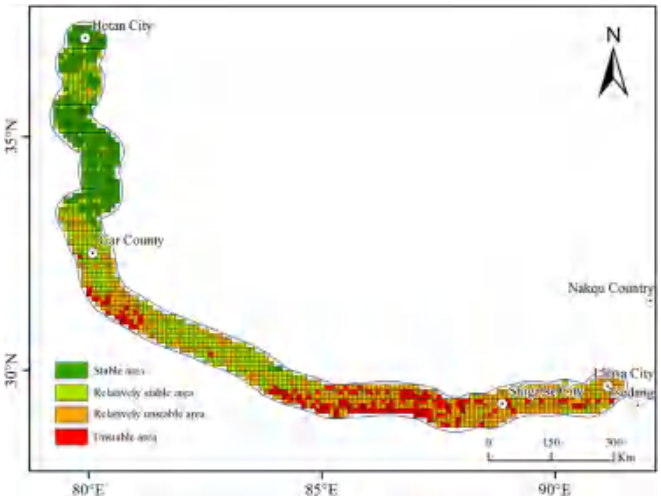

Fig. 2. Crustal Stability Distribution in the 40 km Region Along the Xinjiang-Tibet Railway.

Table 1
Crustal Stability Evaluation Grading Criteria.

Primary Indicator	Secondary Indicator	Unstable (4 points)	Moderately Unstable (3 points)	Moderately Stable (2 points)	Stable (1 point)	Code	Weight
Fault Activity	Active Faults (Vertical Distance)/m	0–500	500–1000	1000–2000	≥2000	L_1	0.0398
Deep Geophysical Features	Bouguer Gravity Anomaly (10^{-5} m/s^2)	−520.54 to −398.69	−398.69 to −276.84	−276.84 to −143.28	−143.28–76.98	L_2	0.0541
Seismic Activity	Historical Earthquake Magnitude/Ms	≥7	6–7	5–6	<5	L_3	0.0533
	Peak Ground Acceleration/g	≥0.4	0.15–0.4	0.05–0.15	≤0.05	L_4	0.0262
Strain Characteristics	Maximum Shear Strain Rate (10^{-8} a^{-1})	20.81–29.31	16.02–20.81	10.75–16.02	4.4–10.75	L_5	0.145
	The Dilatation Rate/ (10^{-8}·a^{-1})	28.41–48.49	19.23–28.41	11.44–19.23	4.34–11.44	L_6	0.1129
Exogenic Dynamic Characteristics	Slope Gradient/°	≥25	15–25	5–15	0–5	L_7	0.0953
	River System Development (Vertical Distance)/m	0–1000	1000–2000	2000–4000	≥4000	L_8	0.1414
	Annual Average Precipitation/ mm	1241.15–2842.75	473.71–1241.15	184.54–473.71	6.58–184.54	L_9	0.1708
	Equivalent Water Height/mm	−100.52 to −54.94	−54.94 to −23.27	−23.27 to −5.52	−5.52 to 22.31	L_{10}	0.1612

0.0582, river system for 0.1516, annual average precipitation for 0.1689, and equivalent water height for 0.1502. For the 170 km region along the railway, the weight distribution is as follows: active faults account for 0.075, Bouguer gravity anomaly for 0.0723, historical earthquake magnitude for 0.1412, peak ground acceleration for 0.0904, maximum shear strain rate for 0.1315, the dilatation rate for 0.0967, slope gradient for 0.1159, river system for 0.063, annual average precipitation for 0.0872, and equivalent water height for 0.1268.

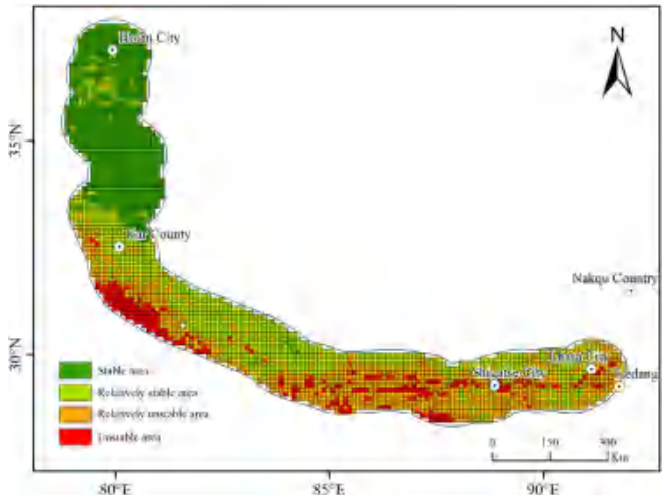

Fig. 3. Crustal Stability Distribution in the 80 km Region Along the Xinjiang-Tibet Railway.

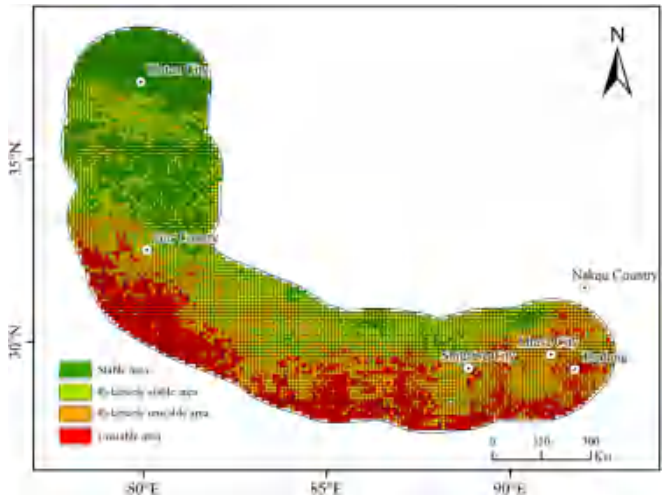

Fig. 4. Crustal Stability Distribution in the 170 km Region Along the Xinjiang-Tibet Railway.

From the table, it is clear that among the five primary indicators, strain characteristics and exogenic dynamic characteristics have relatively high weights. In addition, this study introduces EWH as a new influencing factor. Although precipitation constitutes a critical component of the hydrological cycle, its impact on EWH is mediated through intermediate factors including infiltration capacity, evaporation intensity, and anthropogenic activities, while being regulated by regional geological conditions and vegetation coverage. Consequently, no direct correlation exists between precipitation and EWH. Notably, the classification system designates lower values as unstable regions. The calculated weight of 0.1612, ranking second. This indicates that changes in water storage significantly influence crustal stability. Traditional methods for evaluating crustal stability are limited by fewer influencing factors, yielding more restricted results. By analyzing variations in water storage, trends in regional crustal stability can be observed as the area expands. This also indirectly validates the crustal stability along the Xinjiang-Tibet Railway.

To analyze the crustal stability of areas surrounding the Xinjiang-Tibet Railway and the changes in regional stability as the area expands, we performed a comparative analysis of the results for three different regions. Based on the stability evaluation model, we assessed the crustal stability of the Xinjiang-Tibet Railway in the 40 km, 80 km, and 170 km surrounding areas (Figs. 2–4) and the distribution of stability zones in these areas (Table 2). From Table 2, we observe that in the 40 km study area along the Xinjiang-Tibet Railway, the stable zone occupies 39,563.9 km^2, accounting for 22.87 % of the total area. The moderately stable zone covers 49,666.8 km^2, or 28.71 % of the total area. The moderately unstable zone spans 61,949.5 km^2, or 35.81 % of the total area. The unstable zone covers 21,814.6 km^2, or 12.6 % of the study area. In the 80 km study area, the stable, moderately stable, moderately unstable, and unstable zones occupy 27.61 %, 32.16 %, 31.42 %, and 8.81 % of the total area, respectively. In the 170 km

Table 2
Quantitative Crustal Stability Evaluation and Area Distribution Along the Xinjiang-Tibet Railway.

Stability Level	40 km Area (km^2)	40 km Area Proportion (%)	80 km Area (km^2)	80 km Area Proportion (%)	170 Area (km^2)	170 km Area Proportion (%)
Stable Zone	39563.9	22.87	98042.6	27.61	167667.7	20.96
Moderately Stable Zone	49666.8	28.71	114199.6	32.16	236862.7	29.61
Moderately Unstable Zone	61949.5	35.81	111571.9	31.42	237262.6	29.66
Unstable Zone	21814.6	12.61	31284.2	8.81	158148.5	19.77

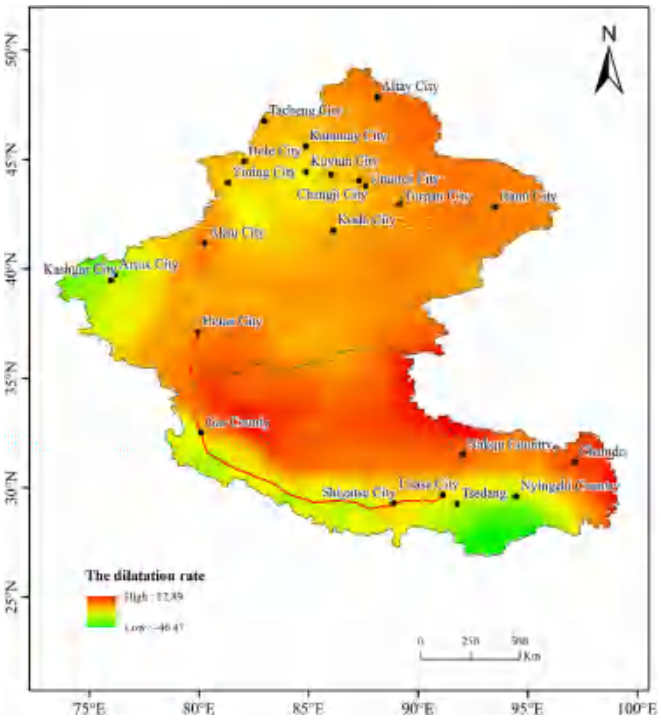

Fig. 5. The variation in the dilatation rate is shown, highlighting its impact on seismic activity.

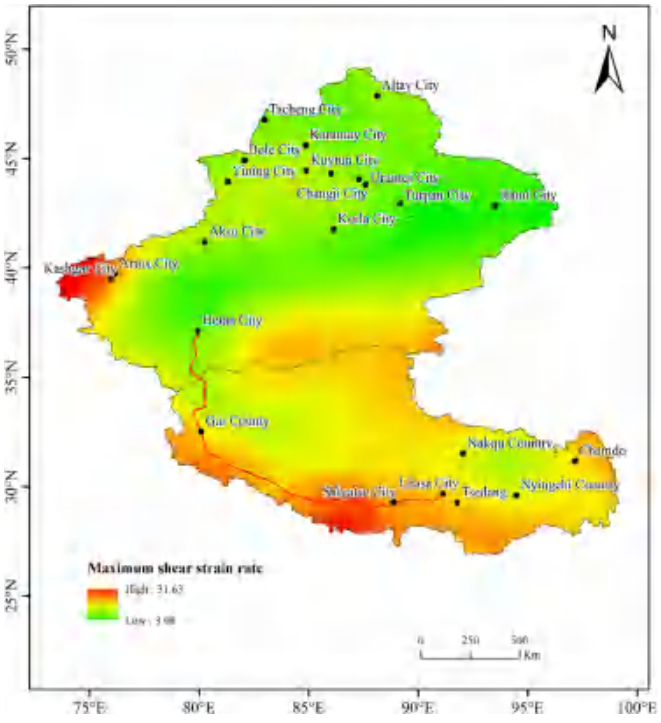

Fig. 6. The variation in the Maximum Shear Strain Rate is shown, highlighting its impact on seismic activity.

study area, the stable, moderately stable, moderately unstable, and unstable zones occupy 20.97 %, 29.61 %, 29.66 %, and 19.77 % of the total area, respectively.

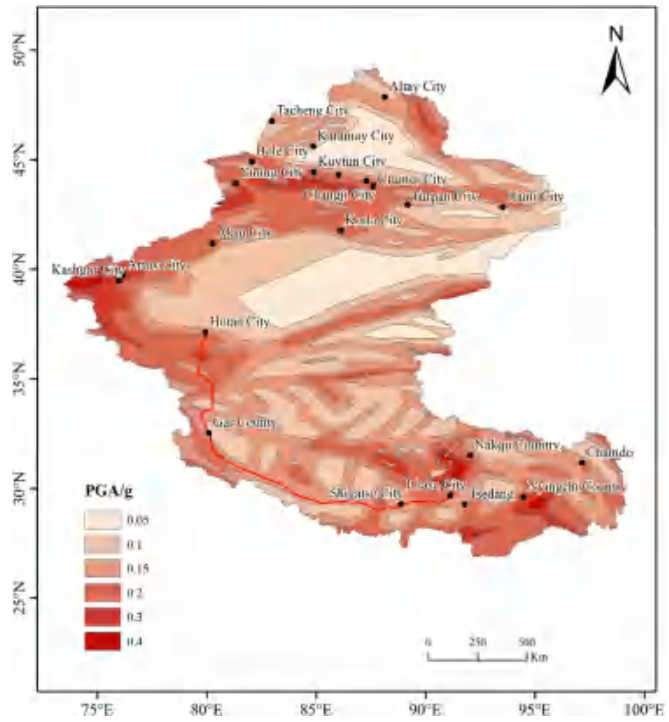

Fig. 7. Peak Ground Acceleration reflects the basic intensity of future seismic events.

From Figs. 2–4, the distribution of crustal stability along the Xinjiang-Tibet Railway follows a block structure, with distinct boundaries between regions. The primary geomorphological feature of the study area is high-altitude mountainous terrain. The colors in the figures represent the following: green for stable zones, cyan for moderately stable zones, orange for moderately unstable zones, and red for unstable zones. The northern section of the Xinjiang-Tibet Railway (from Hetian to Gar County) is predominantly stable or moderately stable, while the southern section (from Gar County to Lhasa) is mainly moderately unstable and unstable. As the study area expands to 80 km and 170 km, the variation in stability levels becomes more pronounced. In the southern section, particularly from Gar County to Lhasa, instability becomes more evident as the area expands. Notably, in the central part of the southern segment, from Gar County to Jilong County, instability is most prominent, with the instability index continuing to increase as we move southward.

From the Bouguer gravity anomaly values (Fig. 12), it is clear that along the Gar County-Lhasa segment, the values range from -465.85×10^{-5} m/s^2 to -106.16×10^{-5} m/s^2. A noticeable color change occurs along the Xinjiang-Tibet Railway route, transitioning from deep blue to indigo, with Bouguer gravity anomaly values shifting from -450.4×10^{-5} m/s^2 to -330×10^{-5} m/s^2. Compared to the surface dilation rate (Fig. 5), the Gar County-Lhasa segment falls within a negative dilation zone, with values ranging

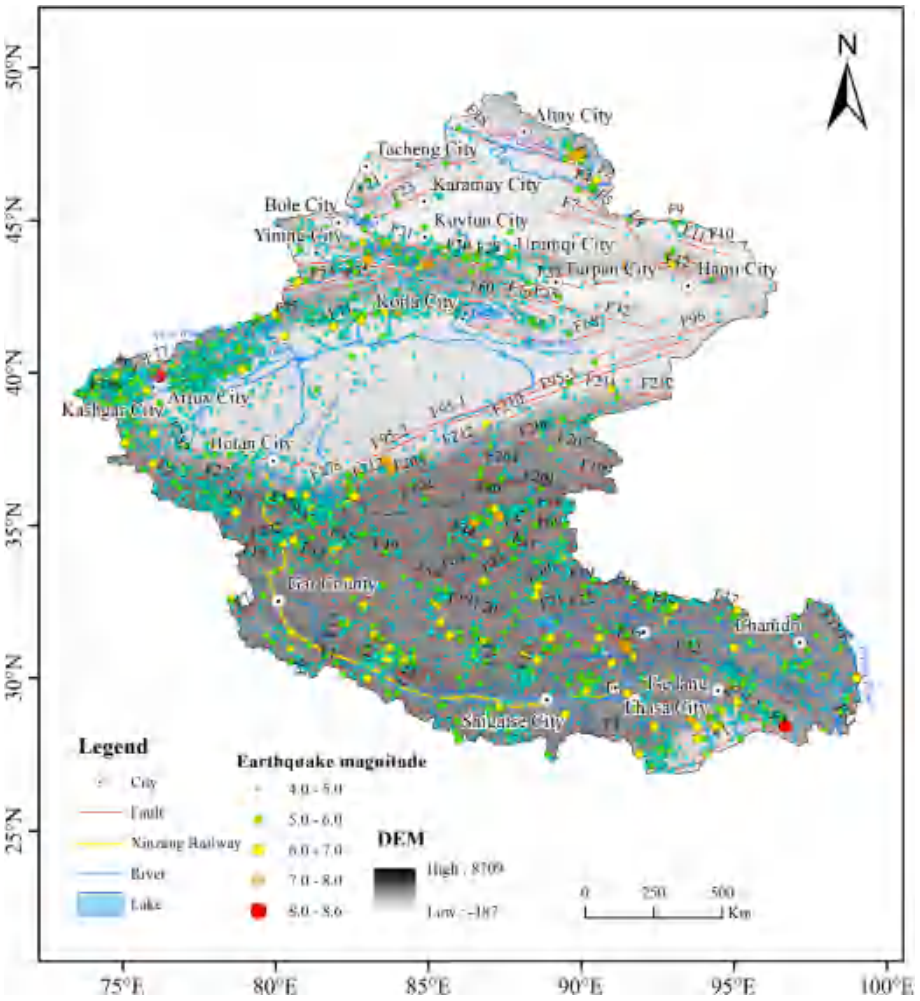

Fig. 8. Earthquake Magnitude and Active Fault Distribution.

from -46.47×10^{-8} to -6.65×10^{-8} m/s^2, influenced by the northern positive dilation zone.

In conjunction with the TWSA trend analysis along the Tibetan Plateau and the Xinjiang-Tibet Railway (Fig. 13), the water storage decline rates for the 40 km and 80 km zones are −4.48 mm/yr and −4.60 mm/yr, respectively. As the area expands to 170 km, the decline rate increases to −5.37 mm/yr. This indicates that with the expansion of the region, the downward trend in water storage intensifies, with the rate of decline increasing by 2.6% from the 40 km to 80 km zone, and by 16.7% from the 80 km to 170 km zone. Notably, the expansion to 170 km marks the region where water storage declines most sharply. Thus, the TWSA variations in the surrounding 40 km and 80 km areas of the Xinjiang-Tibet Railway warrant particular attention.

Fig. 8 shows the distribution of historical earthquake magnitudes and active faults, revealing that the southern section from Gar County to Lhasa is densely populated with fault lines and experiences frequent seismic activity. This region is affected by several faults, including the Qushun Fault, Karakoram Fault, Purang Fault, North Himalaya Normal Fault Zone, Dangre Yongcuo Fault, Yarlung Zangbo River Fault, Jiagang Fault, Musizeng Fault, and Yadong Fault Group. Overall, the design of the Xinjiang-Tibet Railway avoids areas with relatively weak stability. However, unstable areas with frequent seismic activity and complex fault interactions must be carefully evaluated for protective measures during construction.

3.2. Tectonic activity analysis

As shown in Fig. 5, dilatation rates in the Xinjiang-Tibet region are generally evenly distributed, with higher values in the north (mostly above 5×10^{-8} a^{-1}) and lower values in the south, predominantly negative. High dilation values, indicating an extensional state, are observed across most of Xinjiang and northeastern Tibet. Along the Xinjiang-Tibet Railway, including Atushi City in Xinjiang, the dilatation rate reaches a low value of -46×10^{-8} a^{-1}. The western section exhibits lower values in green, while the eastern section shows higher values, with some areas reaching up to 12.89×10^{-8} a^{-1}, creating a clear contrast. This suggests

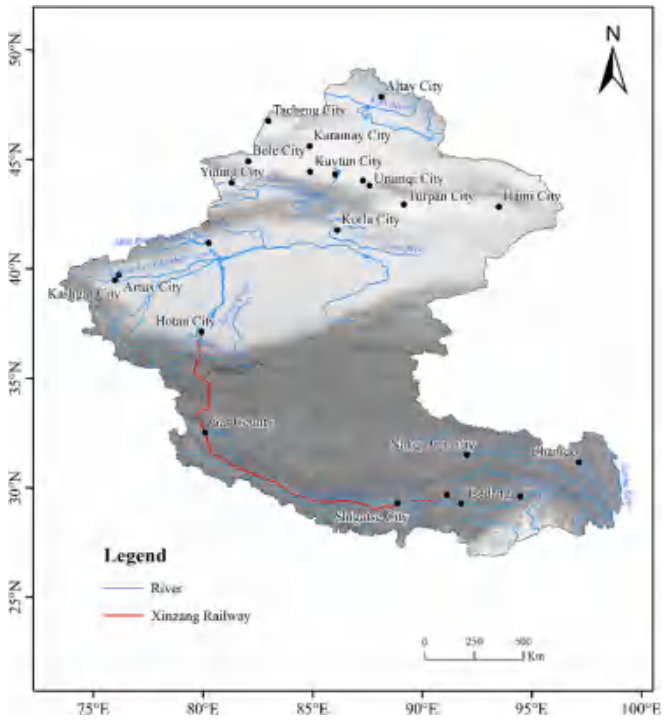

Fig. 9. Major Rivers in the Study Area.

that the eastern region may be more susceptible to seismic activity or experience greater seismic intensity.

Fig. 6 shows the maximum shear strain rate along the Xinjiang-Tibet Railway, starting from a low value of 3.08×10^{-8} a^{-1} in the Hetian region and gradually increasing to moderate values (15×10^{-8} a^{-1}). The rate peaks at 31.63×10^{-8} a^{-1} near the northern Himalayan Front Fault zone, before decreasing to moderate values (16×10^{-8} a^{-1}) as it approaches Lhasa. The color variation along the route clearly highlights regional differences. From Hetian to the Bangong Co fault, the shear strain rate ranges from 3×10^{-8} a^{-1} to 5×10^{-8} a^{-1}. It increases to 10×10^{-8} a^{-1} to 17×10^{-8} a^{-1} near the Karakoram and Himalayan Front Fault zones, reaching high values, especially west of Atushi City and around Shigatse. Notably, the most recent significant earthquake in Tibet, a magnitude 6.8 event in Dingri County, Shigatse, caused substantial damage. The strain rate then gradually decreases to moderate values, though it remains relatively high, emphasizing the need for enhanced seismic risk mitigation between Gar County and Lhasa.

3.3. Seismic results and comprehensive analysis

Earthquakes directly result from fault activity, and PGA indicates the intensity of future seismic events. It is a key factor in evaluating crustal stability. Fig. 7 shows that PGA along the Xinjiang-Tibet Railway ranges from 0.1 g to 0.3 g. From Hetian to Gar County, PGA reaches up to 0.2 g, while from Gar County to Lhasa, it typically ranges from 0.1 g to 0.15 g. In certain areas near Lhasa, PGA can reach up to 0.4 g. Fig. 8 shows the distribution of earthquake magnitudes and active fault zones, indicating that earthquake frequency and magnitude are relatively higher in the Lhasa section. The segment from Hetian to Gar County also experiences a higher frequency of earthquakes, which requires further attention.

Based on data from the National Earthquake Science Data Center (https://data.earthquake.cn), historical earthquake records from 183 BCE to 2023 CE were analyzed, as shown in Fig. 5. Both Xinjiang and Tibet are seismically active regions, with frequent earthquakes of various magnitudes. The seismic activity in these regions is characterized by high frequency and significant intensity. According to the data, there have been 5,791 earthquakes with magnitudes of 4 or greater. Among them, 5,063 had magnitudes between 4 and 5, 573 had magnitudes between 5 and 6, 133 had magnitudes between 6 and 7, and 22 had magnitudes of 7 or greater, including 5 events with magnitudes of 8 or higher. These occurred in Fuyun County, Shawan County, Atushi County in Xinjiang, and Naqu County and Chayu County in Tibet. Along the Xinjiang-Tibet Railway, the sections from Hetian to Gar County and from Shigatse to Lhasa experience relatively high earthquake frequencies, mostly between magnitudes 4 and 6.

3.4. Comprehensive analysis of exogenic factors

Exogenic factors were selected to represent environmental characteristics, including slope gradient, river system development as shown in Fig. 9, and average annual precipitation. Between 2018 and 2022, the annual average precipitation in the Xinjiang-Tibet region ranged from 6.58 mm to 2,842.75 mm. While precipitation is generally evenly distributed across the region, areas such as Cuona County, Motuo County, and Chayu County in Tibet receive exceptionally high rainfall. In contrast, precipitation along the Xinjiang-Tibet Railway is relatively low, as shown in Fig. 10. The slope gradient in the Xinjiang-Tibet region is generally evenly distributed. High-gradient areas are mostly found in mountainous regions, such as the Altai Mountains, Kunlun Mountains, Bolo Kalou Mountains, Altyn-Tagh Mountains, and the Himalayas. The section from Hetian to the Kunlun Mountains and around Lhasa features moderate slopes, with some areas exceeding 35° as shown in Fig. 11. Overall, however, the slope gradient remains relatively gentle.

3.5. Gravity and terrestrial water storage anomalies

Deep structural features, such as gravity anomalies, deep faults, and crustal structure, are key factors in controlling crustal stability. Regional Bouguer gravity anomalies result from variations in the density of underground rocks, geological structures, and morphological changes, reflecting the combined effects of subsurface material. The contours of Bouguer gravity anomalies show high density and regional characteristics, primarily indicating the

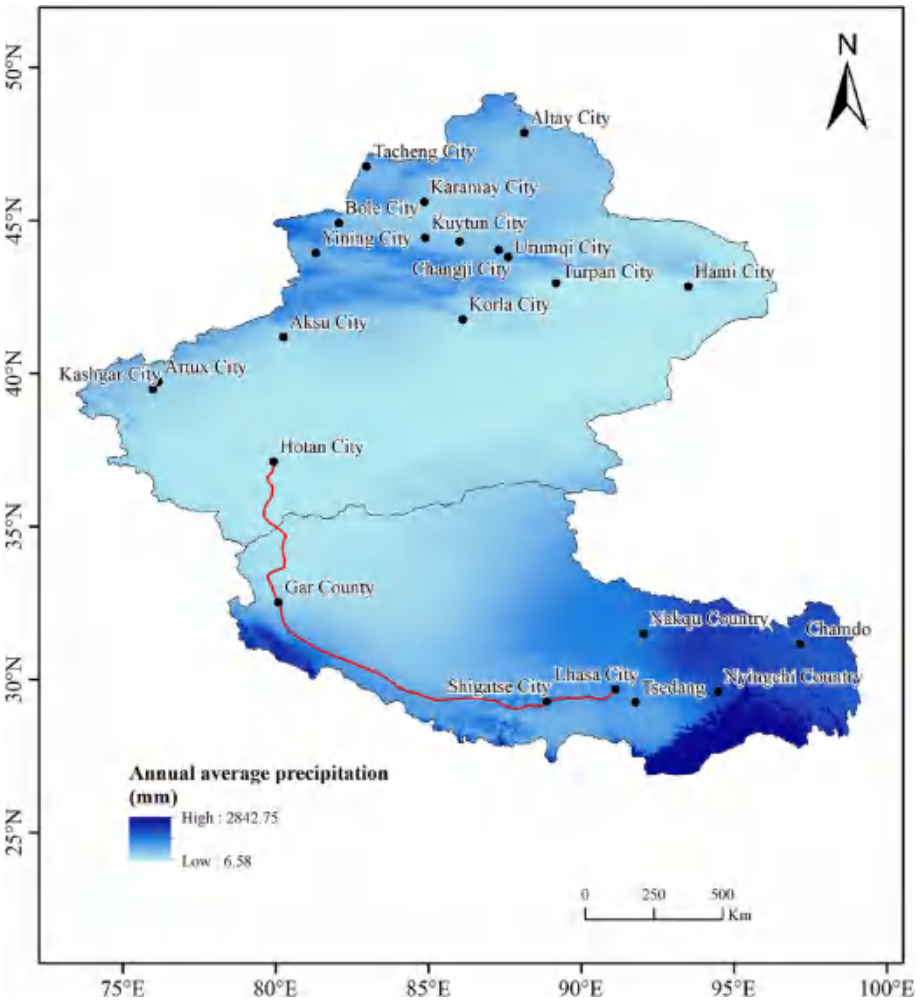

Fig. 10. Average Precipitation from 2018 to 2022.

presence of deep faults. In deep fault zones, the Bouguer gravity anomaly contours form a dense, band-like pattern. Conversely, regions with a gentle gradient suggest the absence of deep crustal fractures. Gravity gradient belts are closely associated with deep faults and seismic zones, and regions with higher gravity anomaly gradients are generally linked to more intense endogenic geological activity, which corresponds to poorer crustal stability.

Using Bouguer gravity anomaly data from Xinjiang and Tibet, we mapped the region's gravity anomaly distribution. Bouguer gravity anomalies range from -520.54×10^{-5} m/s^2 to 9.46×10^{-5} m/s^2, decreasing from north to south. The northern regions show higher values (0 to 9.46×10^{-5} m/s^2), while the southern regions exhibit lower values, mostly around -500×10^{-5} m/s^2. The southern part of Tibet, especially Linzhi County, displays further increases. As shown in Fig. 12, the Xinjiang-Tibet Railway lies within a low-value gravity anomaly area, with a clear north–south trend: higher values in the north and lower values in the south. The gravity anomaly is higher from Hetian to the Kunlun Mountains, but most of the railway is in a low-value region, suggesting a relatively thick and stable crust in this area.

In Fig. 13, panels (c), (e), and (g) show the spatial distribution of TWS anomalies in the 40 km, 80 km, and 170 km surrounding areas of the Xinjiang-Tibet Railway. The trends of Equivalent Water Height (EWH) along the Tibetan Plateau and the Xinjiang-Tibet Railway exhibit a general decline. Panel (a) indicates two distinct regions of water storage changes: an increase in the northern part and a decrease in the southern part of the plateau. Despite these regional differences, the overall interannual variations remain relatively stable, with a slight decline of 0.59 mm per year, as shown in panel (b). The railway route was designed to avoid regions with significant water storage changes in the northern and southern Tibetan Plateau, as well as the southwestern plateau. Most areas surrounding the railway exhibit stable water storage, with a noticeable decline occurring only in the last third of the route. This decline is the main factor contributing to the downward trend in water storage observed in the 40 km, 80 km, and 170 km surrounding areas of the Xinjiang-Tibet Railway.

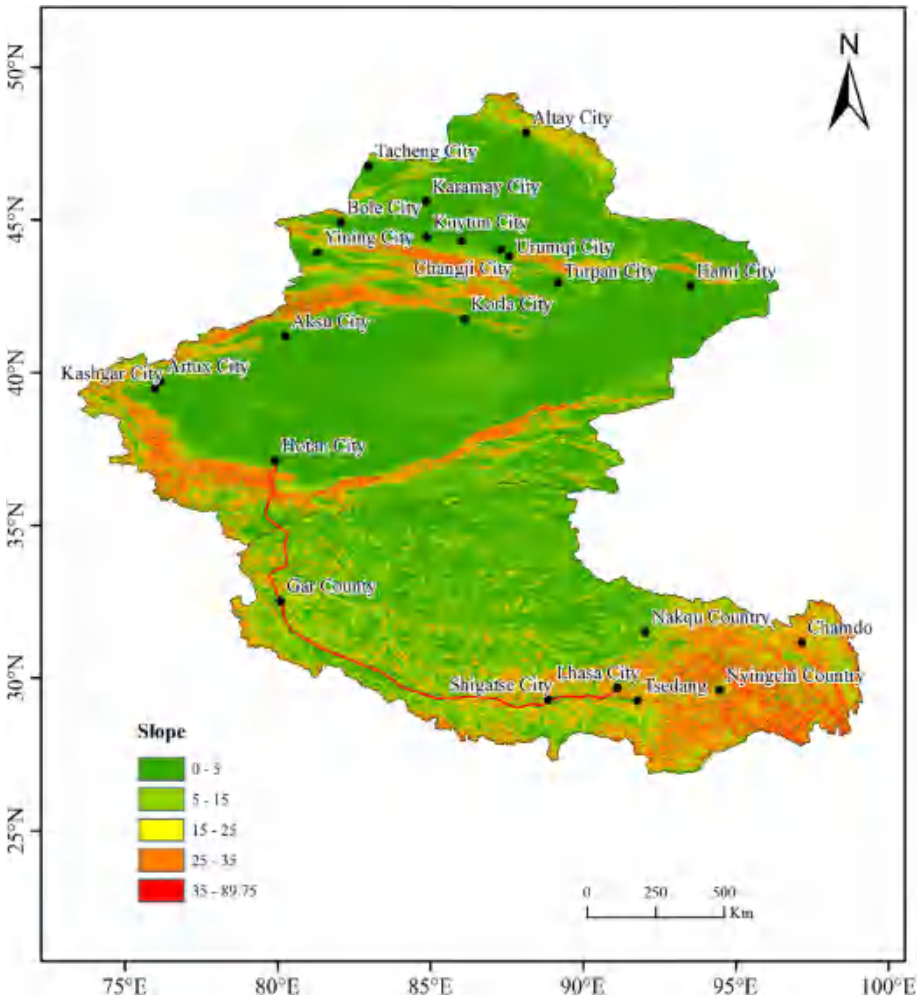

Fig. 11. Slope Overview of the Study Area.

4. Conclusions and discussion

This study presents a multidimensional crustal stability monitoring framework and risk evaluation tool. The results show that the stability levels along the railway are well-defined, with a balanced distribution of stable, moderately stable, unstable, and moderately unstable areas. The unstable regions are primarily located at the southern end of the Gar County to Lhasa section. These unstable zones are mainly along the Northern Himalayan Normal Fault Zone, Dangre Yongcuo Fault, and Yarlung Zangbo River Fault. Comparison of the historical earthquake magnitude distribution shows that earthquakes of magnitude 6 and above predominantly occur in the southern and western regions, aligning with the crustal stability map from this study. Due to the unique geographical location and fragile ecological environment of the Xinjiang-Tibet Railway, this study presents a trend map of terrestrial water storage changes along the Tibetan Plateau and Xinjiang-Tibet Railway. Analysis of equivalent water height (EWH) trends shows that interannual changes in this region are relatively stable, with the overall terrestrial water storage anomaly (TWSA) showing a slight downward trend of 0.59 mm per year. Special attention should be given to the TWSA changes within the 40 km and 80 km surrounding areas of the Xinjiang-Tibet Railway. According to Qu et al. (2010), no significant active or quiet periods have been observed in the Western Kunlun earthquake belt, and its seismic activity remains relatively subdued. Similarly, Hu et al. (2013) analyzed continuous GPS observations and found minimal overall deformation along the Tarim Basin's edge, confirming the stability of the region. These findings are consistent with this study, where the Hetian area and the surrounding 170 km of the Xinjiang-Tibet Railway are classified as stable zones. Additionally, stress measurements in the Lhasa block (Meng et al.,2017; Zhang et al., 2017) indicate that horizontal stress in the Lhasa block is significantly stronger than vertical stress, and stress accumulation in the Linzhi region has not been fully released since the Nepal earthquake. This suggests a potential geological hazard risk, consistent with the instability observed in the Lhasa section, where surrounding areas are categorized as unstable or moderately unstable.

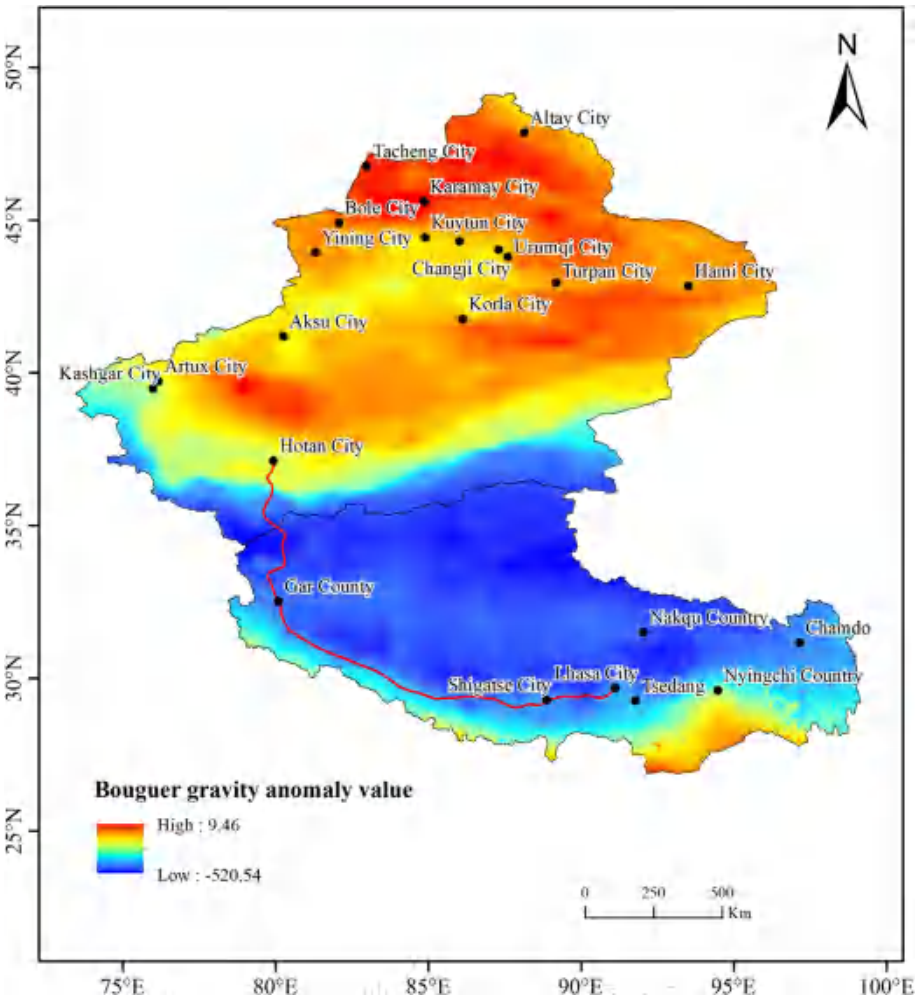

Fig. 12. Bouguer Gravity Anomaly Values.

Based on a holistic consideration of regional crustal stability evaluation, we expand the study area to 170 km. However, minor discrepancies are observed in specific regions among the three analysis results, necessitating more detailed investigation. To ensure analytical consistency, we reclassify the results from the two smaller study areas (40 km and 80 km) according to the 170 km regional classification criteria, as illustrated in Fig. 14. Comparative analysis of Fig. 14b, f, and j reveals distinct spatial patterns near Hetian County. Both Fig. 14b and 14f demonstrate consistency, indicating predominantly stable conditions in Hotan County with localized relatively stable zones. In contrast, Fig. 14j exhibits increased proportions of relatively stable areas, with stable zones confined to northern Hetian County. Near Rikeze City, the results of the three study areas are consistent (Fig. 14c, g, and k). Notably, the 170 km result (Fig. 14k) presents enhanced informational richness compared to the 40 km and 80 km results (Fig. 14c, g), effectively validating the necessity of study area expansion. However, in the Lazhi-Saga segment west of Rikeze City, Fig. 14k reveals concentrated unstable zones within relatively unstable areas, whereas Fig. 14c and g primarily show homogeneous relatively unstable distributions. Significant discrepancies emerge in the Rikeze-Lhasa, where Fig. 14c and g display relatively unstable areas interspersed with relatively stable zones, while Fig. 14k exhibits predominantly relatively unstable regions with localized unstable clusters. Analysis of the Zhongba-Geer segment (Fig. 14d, h, l) demonstrates that the 40 km and 80 km results present relatively stable areas containing unstable subzones, whereas the 170 km results reveal alternating relatively unstable and relatively stable zones with embedded unstable regions. Collectively, the 170 km results provide transitional refinement between the 40 km and 80 km outcomes, revealing enhanced spatial detail and three-dimensional stability distribution patterns.

To validate model effectiveness, we incorporated seismic data from the 2024 earthquake catalog (Fig. 14i), recording 45 earthquakes with magnitudes ≥ 3 within the study area. Notably, 21 events (46.7 %) occurred in relatively unstable and unstable zones along the Xinjiang-Tibet Railway corridor, substantiating the practical relevance of our evaluation results. This spatial correlation between seismic activity and identified unstable zones provides empirical support for the model's predictive capability in regional crustal stability assessment.

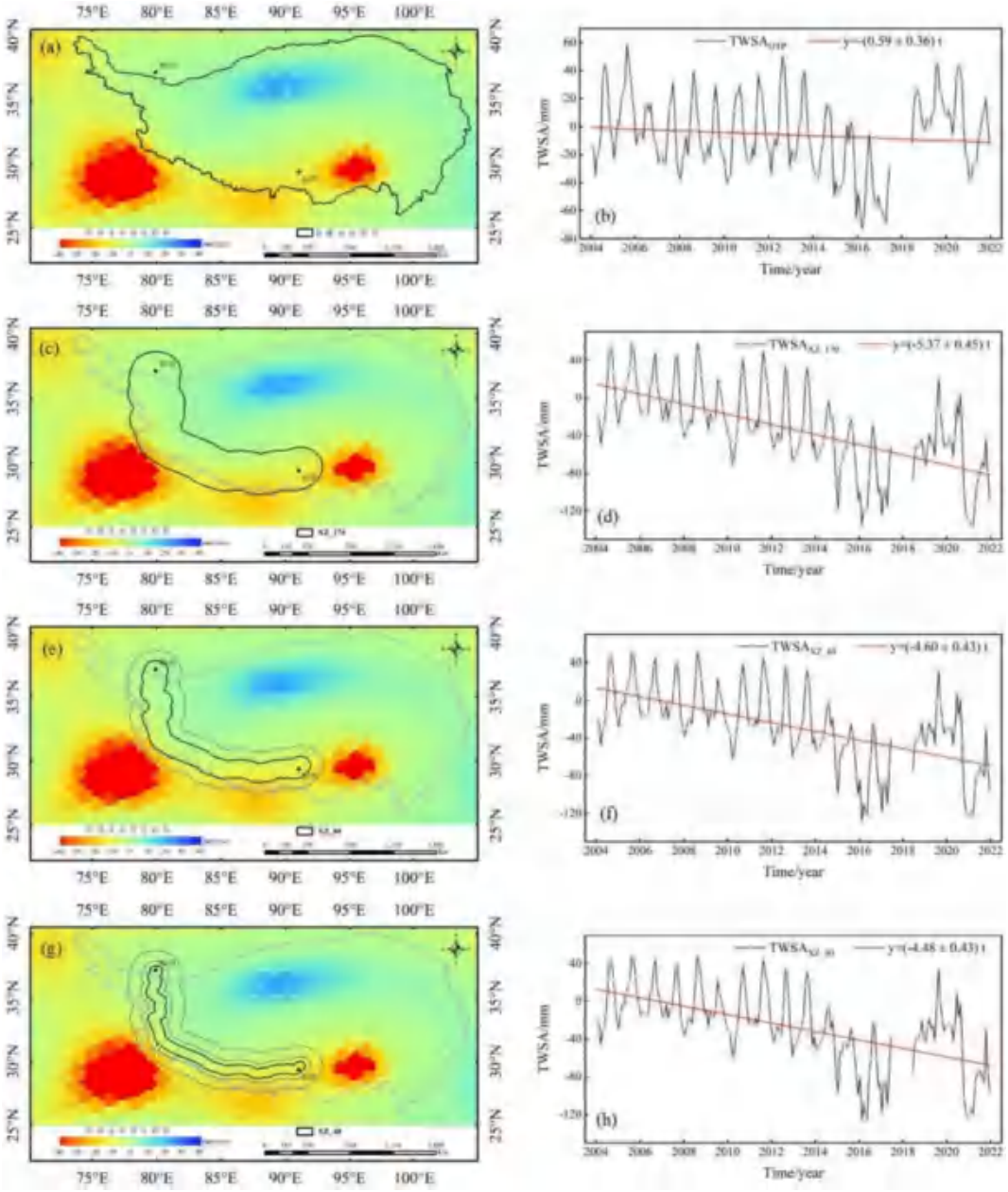

Fig. 13. TWSA Change Trends Along the Tibetan Plateau and Xinjiang-Tibet Railway.

Monitoring and assessing regional crustal stability is an evolving field in Earth science. The use of high-precision geodetic data, combined with seismic, geological, and hydrological data, along with emerging monitoring technologies, has significantly improved assessments. As geodetic data continues to advance, evaluations will become more refined. However, despite these advancements, several challenges remain in the development of evaluation systems, including insufficient indicators, imbalanced weight distribution, lack of methods for data integration, and limited application of results. Crustal stability involves complex interactions between multiple physical processes and exogenic factors, but current evaluation systems often treat these factors in isolation, without addressing their interrelationships. Furthermore, many existing systems rely on static data or incomplete temporal data, which can introduce errors and limit the system's ability to predict future trends or respond to emergencies. Therefore, evaluation indicators and methods for monitoring crustal stability must continue to evolve and improve.

Data availability

Data will be made available on request. The earthquake magnitude data is sourced from the National Earth System Science Data Center, National Science and Technology Infrastructure Platform (http://www.geodata.cn).

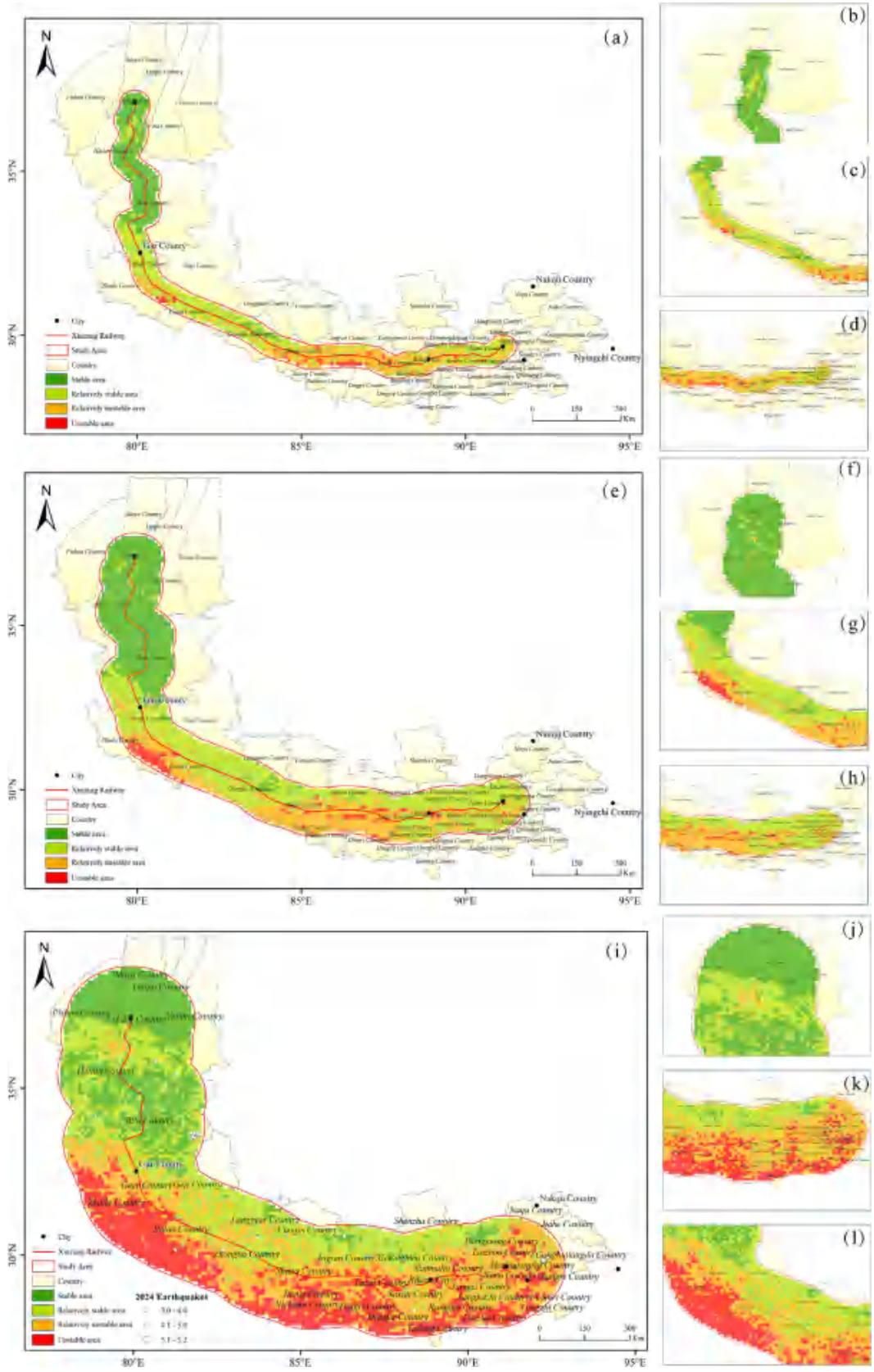

Fig. 14. Multi-Scale Verification of Crustal Stability Zonation: High-Resolution Terrain Analysis Along the Xinjiang-Tibet Railway Engineering Corridor.

Declaration of competing interest

The authors declare that they have no known competing financial interests or personal relationships that could have appeared to influence the work reported in this paper.

Acknowledgements

This work was supported in part by the Tianjin Key Laboratory for Rail Transit Navigation Positioning and Spatial-Temporal Big Data Technology (Grant No. TKL2023B05), the Science and Technology Research and Development Project of China State Railway Group Co., Ltd (Grant No. Q2023T004), and the Natural Science Foundation of Henan Province (Grant No. 232300421401).

References

Bogdanova, I., Vandergheynst, P., Antoine, J., et al., 2005. Stereographic wavelet frames on the sphere. Appl. Comput. Harmon. Anal. 19 (2), 223–252.

Chen, B., Qu, W., Zhang, Q., et al., 2022. Current crustal deformation and multi-scale strain rate field characteristics in the southeastern margin of the Tibetan Plateau. J. Geodyn. Earth Dyn. 42 (10), 1047–1055.

Dang, Y., Yang, Q., Wang, W., 2017. Methods and applications of geodetic monitoring for regional geological environment stability. J. Geodesy Sci. 46 (10), 1336–1345.

Eshagh, M., Jin, S.G., Pail, R., Barzaghi, R., Tsoulis, D., Tenzer, R., Novak, P., 2024. Satellite gravimetry: methods, products, applications and future trends. Earth Sci. Rev. 253. 104783.

Franklin, K.R., Huang, M.H., 2022. Revealing crustal deformation and strain rate in Taiwan using InSAR and GNSS. Geophys. Res. Lett. 49 (21). e2022GL101306. https://doi.org/10.1029/2022GL101306.

Heki, K., Jin, S., 2023. Geodetic study on Earth surface loading with GNSS and GRACE. Satell. Navig. 4, 24.

Hu, Y., Hao, M., Li, Y., et al., 2013. Current crustal deformation and seismic activity in Xinjiang. J. Seismol. 35 (6), 820–827, + 938.

Jin, S.G., Wang, J., Park, P.H., 2005. An improvement of GPS height estimates: stochastic modeling. Earth Planets Space 57 (4), 253–259. https://doi.org/10.1186/BF03352561.

Jin, S.G., Luo, O.F., Ren, C., 2010. Effects of physical correlations on long-distance GPS positioning and zenith tropospheric delay estimates. Adv. Space Res. 46 (2), 190–195. https://doi.org/10.1016/j.asr.2010.01.017.

Jin, S.G., Wang, Q., Dardanelli, G., 2022. A review on multi-GNSS for Earth observation and emerging applications. Remote Sens. 14 (16). 3930. https://doi.org/10.3390/rs14163930.

Jin, S.G., Camps, A., Jia, Y., Wang, F., Martin-Neira, M., Huang, F., Yan, Q., Zhang, S., Li, Z., Edokossi, K., Yang, D., Xiao, Z., Ma, Z., Bai, W., 2024. Remote sensing and its applications using GNSS reflected signals: advances and prospects. Satell. Navig. 5, 19. https://doi.org/10.1186/s43020-024-00139-4.

Liu, X., Xu, K., Wang, X., et al., 2023. Crustal stability monitoring and assessment along the Red River Fault Zone using GNSS. Sci. Surv. Mapp. 48 (4), 68–78. https://doi.org/10.16251/j.cnki.1009-2307.2023.04.008.

Meng, W., Guo, C., Zhang, Z., et al., 2017. Crustal stress measurements of the Lhasa block in the Tibetan Plateau and their significance. Geophys. J. Int. 60 (6), 2159–2171.

Pan, Y. et al., 2023. Interannual variability of vertical land motion over High Mountain Central Asia from GPS and GRACE/GRACE-FO observations. GPS Solut. 27 (4), 168.

Qu, Y., Wang, Q., Nie, X., 2010. Tectonic zones and seismic activity in southern Xinjiang. Seismol. Geol. 24 (4), 298–306. https://doi.org/10.16256/j.issn.1001-8956.2010.04.002.

Rao, W., Sun, W., 2020. Moho interface changes beneath the Tibetan Plateau based on GRACE data. J. Geophys. Res.: Solid Earth 126. e2020JB020605. https://doi.org/10.1029/2020JB020605.

Wu, J., 2024. Fault characteristics and regional crustal stability study in the Bailongjiang River Basin [D]. Lanzhou University.

Xu, C., Xiong, W., Liu, C., 2023. Progress in three-dimensional crustal deformation and seismic hazard assessment of the Tibetan Plateau using geodetic data. J. Wuhan Univ. Inf. Sci. Eng. 48 (7), 997–1009.

Yao, X., Zhang, L., Li, L., et al., 2021. InSAR evaluation of crustal stability in engineering site regions. Eng. Geol. J. 29 (1), 104–115.

Zhang, Y., Wu, R., Guo, C., et al., 2022. Geological safety assessment for railway engineering in plateau mountainous areas: ideas and methods. Acta Geologica Sinica 96 (5), 1736–1751. https://doi.org/10.19762/j.cnki.dizhixuebao.2022039.

Zhang, P.Z., Deng, Q.D., Zhang, Z.Q., et al., 2013. Active faults, earthquake hazards, and geodynamic processes in the continental China. Science China Earth Sciences 43 (10), 1607–1620.

Zhang, P., Qu, Y., Guo, C., et al., 2017. Stress measurement monitoring in Linzhi, Tibet, and response analysis of the Nepal M8.1 earthquake. Mod. Geol. 31 (5), 900–910.

Zhao, Q., Wu, W., Wu, Y., 2017. Using combined GRACE and GPS data to investigate vertical crustal deformation at the northeastern margin of the Tibetan Plateau. J. Asian Earth Sci. 134, 122–129. https://doi.org/10.1016/j.jseaes.2016.11.010.

Xu, K., Liu, J., Liu, X., et al., 2020. Multiscale crustal deformation around the southeastern margin of the Tibetan Plateau from GNSS observations. Geophys. J. Int. 223 (3), 1188–1209.

Further reading

Cao, X., Li, S., Xu, L., et al., 2015. Mesozoic–Cenozoic evolution and mechanism of tectonic geomorphology in the central North China Block: constraint from apatite fission track thermochronology. J. Asian Earth Sci. 114 (15 Pt.1), 41–53.

Chen, L., Mei, L., Zeng, B., et al., 2020. Failure probability assessment of landslides triggered by earthquakes and rainfall: a case study in Yadong County, Tibet, China. Sci. Rep. 10, 16531. https://doi.org/10.1038/s41598-020-73727-4.

Deng, Q., Cheng, S., Ma, J., et al., 2014. Seismic activity and current seismic situation in the Tibetan Plateau. Geophys. J. Earth Sci. 57 (7), 2025–2042.

Jiao, J., Pan, Y., Ren, D., Zhang, X., 2024. Present-day three-dimensional crustal deformation velocity of the Tibetan Plateau due to multi-component land water loading. Geophys. Res. Lett. 51. e2024GL108684.

Lai, Y., Zhang, B., Yao, Y., et al., 2022. Quantitatively analyzing the impacts of seasonal water storage changes in the Three Gorges Reservoir on nearby crust. Pure Appl. Geophys. 179, 817–831. https://doi.org/10.1007/s00024-021-02928-3.

Ling, H.I., Cheng, H.D., 1997. Rock sliding induced by seismic force. Int. J. Rock Mech. Min. Sci. 34 (6), 1021–1029.

Li, C., Zhang, J., Philbin, S.P., et al., 2022. Evaluating the impact of highway construction projects on landscape ecological risks in high-altitude plateaus. Sci. Rep. 12. 5170. https://doi.org/10.1038/s41598-022-08788-8.

Long, D., Shen, Y., Sun, A., et al., 2014. Drought and flood monitoring for a large karst plateau in Southwest China using extended GRACE data. Remote Sens. Environ. 155, 145–160.

Lv, M., Chen, K., Chai, H., et al., 2022. Joint InSAR and high-frequency GNSS displacement waveform inversion of the 2022 Menyuan M6.9 earthquake coseismic rupture process. Geophys. J. Int. 65 (12), 4725–4738.

Syed, T.H., Famiglietti, J.S., Rodell, M., et al., 2008. Analysis of terrestrial water storage changes from GRACE and GLDAS. Water Resour. Res. 44 (2).

Wang, H., Tan, C., Feng, C., et al., 2022. Active tectonics and crustal stability in the Beijing-Tianjin-Hebei coordinated development area. Geol. Bull. 41 (8), 1322–1341.

Xie, J., Xu, Y., Wang, Y., et al., 2019. Influences of climatic variability and human activities on terrestrial water storage variations across the Yellow River basin in the recent decade. J. Hydrol. 579. 124218.

Xu, J., Zeng, X., 2024. Stress modeling for the upper and lower crust along the Anninghe, Xianshuihe, and Longmenshan Faults in southeastern Tibetan Plateau. Front. Earth Sci. 121439493.

Zhang, P., Deng, Q., Zhang, G., et al., 2003. Active tectonic blocks and strong earthquakes in the continent of China. Sci. China Ser. D Earth Sci. 46 (Suppl. 2), 13–24.

Zhang, L., Sun, W., 2022. Applications of GRACE Mascon products: progress and outlook. Earth Planet. Sci. Rev. 53 (1), 35–52.

Zhang, C., Zhang, S., Yang, W., Meng, H., Lyu, J., Zhang, T., Wu, J., Guo, H., 2021. Assessment of regional crustal stability in Shenfu New Area of Liaoning Province, China. J. Geomech. 27 (3), 453–462.

Zhao, Q., Wu, W., Wu, Y., 2022. Seismic hazard evaluation of crustal stability in the Tibetan Plateau. Earthq. Sci. 35 (5), 1245–1257.

Zhou, G., Zhang, J., Wang, S., 2023. Crustal deformation along the Sichuan-Tibet Railway based on GPS measurements. Geodesy Geophys. 59 (2), 215–227.

Zhu, C., Liu, Y., Chen, Z., et al., 2015. Crustal stability evaluation based on multi-factor analysis: a case study of the Yunnan-Tibet Railway. Geophys. J. Int. 61 (3), 456–465.

Zhu, Z., Zhang, Z., Hu, Y., et al., 2018. Long-term crustal motion in the Eastern Himalayas based on geodetic observations. Geophys. Res. Lett. 45 (6), 2234–2247.

Zhu, X., Zhang, Y., Jiang, L., et al., 2020. Gravity anomaly analysis of crustal stability in the eastern Tibetan Plateau. J. Geodyn. 60, 223–234.